Engineering Structures 31 (2009) 2060–2069

Contents lists available at ScienceDirect

Engineering Structures

journal homepage: www.elsevier.com/locate/engstruct

Blast testing of ultra-high performance fibre and FRP-retrofitted concrete slabs

C. Wu [a,*], D.J. Oehlers [a], M. Rebentrost [b], J. Leach [c], A.S. Whittaker [d]

[a] School of Civil, Environmental and Mining Engineering, The University of Adelaide, SA, Australia

[b] VSL Australia Pty Ltd, Australia

[c] Weapons Systems Division, Defence Science and Technology Organisation, Australia

[d] Department of Civil, Structural and Environmental Engineering, State University of New York, Buffalo, USA

ARTICLE INFO

Article history:
Received 20 May 2008
Received in revised form
11 March 2009
Accepted 11 March 2009
Available online 19 April 2009

Keywords:
Blast testing
Ultra-high performance fibre concrete
FRP
Reinforced concrete

ABSTRACT

A series of tests was conducted to investigate the blast resistances of slabs constructed with both plain ultra-high performance fibre concrete (UHPFC) and reinforced ultra-high performance fibre concrete (RUHPFC), and slabs reinforced with externally bonded (EB) fibre reinforced polymer (FRP) plates. Normal reinforced concrete (NRC) slabs were tested as control specimens. LVDTs and pressure transducers were used to record deflection histories, and pressure sensors located at the centre and one edge of the slabs measured airblast pressure histories. The measured pressures at the centre and edge of the slabs were significantly different from those estimated using traditional procedures such as those in TM5-1300. Tests indicated that the plain UHPFC slab had a similar blast resistance to the NRC slab and that the RUHPFC slab was superior to both. The addition of EB carbon FRP plates to the compression face of a reinforced concrete slab increased its ductility and blast resistance. Test results were compared with the maximum energy absorptions predicted from layered capacity analyses of the NRC, retrofitted, plain UHPFC, and RUHPFC specimens.

1. Introduction

Terrorist attacks using improvised explosive devices (IED) can result in the collapse of buildings, bridges and infrastructure and great loss of life (e.g.,[1–4]). To mitigate the effects of airblast loads on buildings, cost-effective structural-engineering solutions may include: retrofitting using externally bonded (EB) or near surface mounted (NSM) FRP plates to strengthen existing structural members [5–9]; or the use of innovative materials such as ultra-high performance fibre concrete (UHPFC) for the construction of new structural members.

Ultra-high performance fibre concrete (UHPFC) is a relatively new construction material with higher strength, deformation capacity and toughness than conventional normal strength, normal weight concrete. These superior material properties are achieved by adding small steel fibres into the concrete mix that results in concrete compressive strengths in excess of 150 MPa, tensile capacities of approximately 30 MPa and much greater ductility than normal strength, normal weight concrete. Sample stress–strain curves for UHPFC materials are shown in Fig. 1. UHPFC has been used in structural elements to resist extreme earthquake effects [10], blast loads and ballistic loads ([11–13]), and in high-performance structures [14]. The mechanical characteristics and high density of UHPFC make it an ideal material for resisting blast effects, but only a few tests have been conducted to characterize the blast resistance of the plain UHPFC and RUHPFC members ([15,13]).

Blast tests of FRP-retrofitted RC members have been conducted recently [16–18]. Muzsynski and Purcell [17] conducted a series of full-scale explosive tests on RC walls, retrofitted with either EB CFRP (carbon fibre reinforced polymer) or GFRP (glass fibre reinforced polymer) on the rear (tensile) face, using 860 kg of TNT at relatively small standoff distances (between 11–15 m). They observed that the two retrofitted walls had a higher blast resistance and generally performed better than the control walls. Another set of tests on reinforced concrete panels retrofitted with either EB CFRP or GFRP on the front and rear surfaces, which were subjected to blast loadings from charge weights of 13 to 33 kg of ANFO explosives (approximately 80% efficiency of TNT) at a standoff distance of 3 m, was reported by Tolba [31]. Tolba's test results showed that the FRP-retrofitted panels were able to withstand high pressures and displacements without failing, which was in direct contrast to the control panels that failed in shear. Lu et al. [18] conducted blast tests on four EB-FRP-retrofitted slabs. Two were retrofitted on the tension surface only and two were retrofitted on both surfaces. The blast tests were conducted at a standoff distance of 300 mm. The slabs retrofitted on only one surface were damaged severely. Lu concluded that applying plates

* Corresponding author.
E-mail address: cwu@civeng.adelaide.edu.au (C. Wu).

0141-0296/$ – see front matter © 2009 Elsevier Ltd. All rights reserved.
doi:10.1016/j.engstruct.2009.03.020

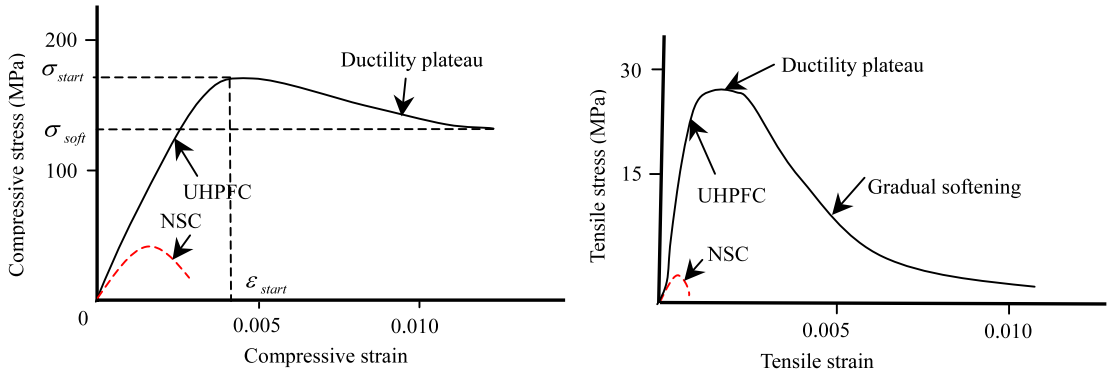

Fig. 1. Mechanical properties of conventional concrete and UHPFC.

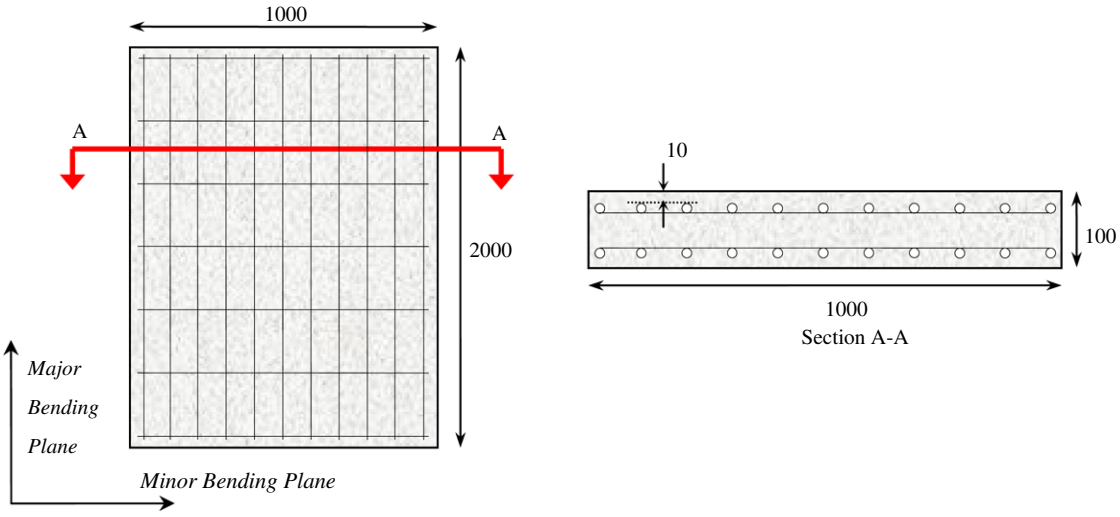

Fig. 2. Geometry of the control specimens.

to both sides of the slab was more effective than applying plates to the tension surface only. They did not investigate the effect of plating on the compression surface only. Wu et al. [19] conducted blast tests on two RC slabs. The first conventionally reinforced slab was used as a control specimen; the second slab was retrofitted with 6 NSM FRP strips on both faces. Each specimen was subjected to two blast detonations with the equivalent of 0.08 kg and 2.1 kg of TNT at a standoff distance of 0.6 m. The test results showed that the specimen with the NSM strengthened tensile face did not withstand a higher blast pressure (impulse) than the conventional specimen; this indicated that only using tension face plates was not effective against blast loading. No investigation of the effectiveness of compressive face retrofitting of RC slab has been reported.

Cramsey and Naito [20] subjected four precast concrete wall panels to a series of far-field blast loadings that produced peak reflected pressures (impulses) of between 55 kPa (476 kPa ms) and 200 kPa (992 kPa ms). These panels consisted of two conventional control specimens, one solid-zone sandwich panel and one C-grid sandwich panel. The sandwich panels were conventional, insulated precast concrete wall panels constructed with welded wire fabric and prestressing strand. The authors noted that cracking was more extensive in the control panels; made observations regarding performance using metrics established in US government standards; and developed SDOF models of the panels.

In this study, a total of 6 slabs were tested to determine their response to blast loading. These six slabs consisted of: two conventional reinforced concrete (RC) slabs for control specimens; two reinforced concrete slabs retrofitted with pultruded externally bonded fibre reinforced polymer on the compression face; one slab constructed with ultra-high strength concrete with no steel reinforcement; and one ultra-high strength concrete slab with steel reinforcement. All of the slabs were 2000 × 1000 mm in plan and 100 mm thick. A total of 8 blast shots were conducted on the 6 specimens. Explosive charge sizes ranged from 1 to 20 kg of equivalent TNT Composition B and standoff distances ranged up to 3m. The blast pressure histories on the slab surfaces and displacement histories of the slabs were recorded. The pressure distributions are analyzed and compared with those predicted using weapon-effects codes such as CONWEP [21]. The responses of the slabs were observed and their energy absorption was compared with predictions made using a layered capacity analysis [22].

2. Design of experiments

2.1. Specimen specifications

The reinforced concrete specimens with normal concrete (NCR) in Fig. 2 were reinforced on both the tension and compression faces. These specimens were constructed with a 12 mm diameter mesh that was spaced at 100 mm centres in the major bending plane (ρ = 1.34%) and at 200 mm centres in the minor plane (ρ = 0.74%). The thickness of the concrete cover was 10 mm. The concrete had a cylinder compressive strength of 39.5 MPa, tensile strength of 8.2 MPa and Young's modulus of 28.3 GPa. The reinforcement had a yield strength of 600 MPa and Young's

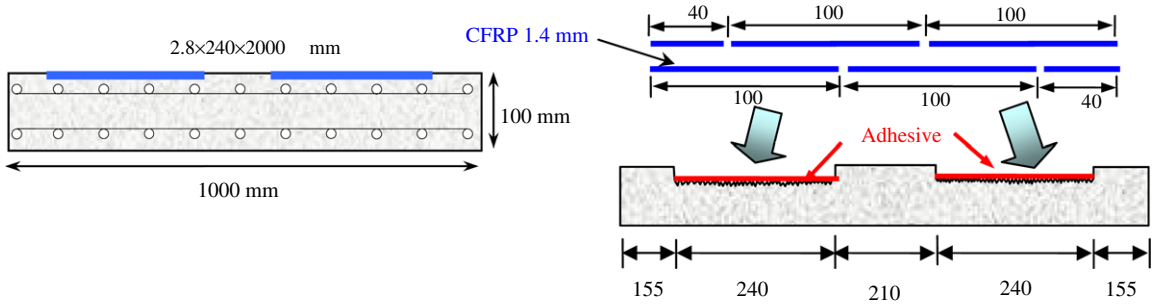

Fig. 3. Geometry of retrofitted slabs (dimensions in mm, [23]).

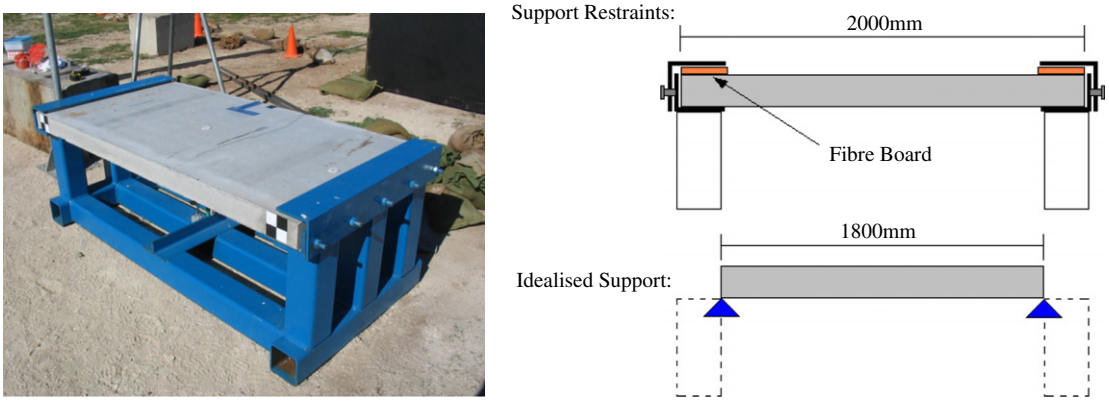

(a) Test fixture. (b) Support conditions.

Fig. 4. Construction details and boundary conditions.

modulus of 200 GPa. Fig. 2 illustrates the conventionally reinforced concrete slabs.

Externally bonded FRP pultruded plates were adhesively bonded to the compression face of a conventionally reinforced slab. Layers of 2.8 mm thick pultruded CFRP plates were used to retrofit the specimens. Fig. 3 presents the cross-sectional properties of the retrofitted slabs. Two 240 mm wide grooves running the length of the slab during manufacturing the slabs were formed to allow for the installation of the pultruded CFRP plates. Two layers of 1.4 mm thick CFRP plates were used in order to achieve a depth of 2.8 mm. Two 100 mm wide and one 40 mm wide plates were used to produce a total width of 240 mm. Fig. 3 provides key construction details. The concrete surface was roughened to improve the quality of the bond to the concrete. After curing concrete for 30 days, the CFRP was attached to the slab.

Two slabs of UHPFC were constructed with and without reinforcement. The RUHPFC slab was constructed with the reinforcement ($\rho = 1.34\%$) in Fig. 2. The ultra-high strength concrete had an average compressive strength of 151.6 MPa, tensile capacity of 30.2 MPa and Young's modulus of 47 GPa at the time of testing.

2.2. Experimental set-up

The specimens were tested on the steel frame in Fig. 4. During testing, bolted angle sections were used to effectively provide an upward restraint against the slab rebound and reduced lateral movement. A firm restraint was formed after fibre boards were wedged into the gap between the slab and the angles but it still maintain the simply supported condition, which was the assumption made in the pre-test calculations. The effective span of the slabs was 1800 mm as shown in Fig. 4.

The support fixture for the explosive charge consisted of three pipe sections as seen in Fig. 5. The charge was suspended from the horizontal section with light rope. The charge was centred over the slab using four string guides.

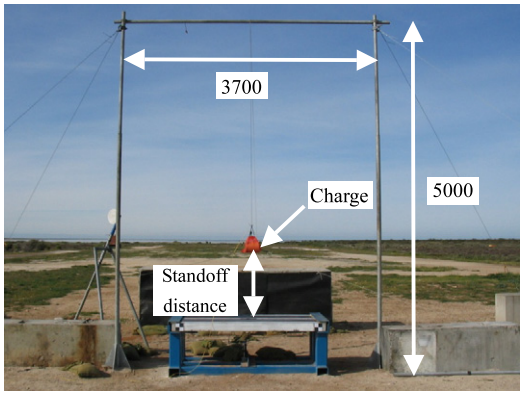

Fig. 5. Charge support frame (dimensions in mm).

2.3. Data acquisition

Data were recorded using a Linear Variable Displacement Transducer (LVDT), pressure transducers, and a high speed camera. Fig. 6 shows the location of the instruments. An LVDT of 250 mm maximum range was installed to record the displacement history at the centre of each slab [23]; the sampling rate was 10 kHz. Pressure transducers were used to measure airblast pressures both at the centre of the specimen (PT1) and near one support (PT2). Blast pressures above 6.9 MPa were not recorded because the transducers were removed to avoid damage at higher pressures. The pressure transducers had a sampling rate of 2 MHz. A high speed camera capturing 2,000 frames per second was used to record each experiment.

Table 1
Experimental airblast program.

Blast	Slab name	Description	Rebar ratio (%)	Standoff distance (m)	Scaled distance (m/kg$^{1/3}$)	Explosive mass (g)
NRC-1	1A	RC	1.34	3	3.0	1007
NRC-2	1A	RC	1.34	3	1.5	8139
NRC-3	1B	RC	1.34	1.4	0.93	3440
NRC-4	1A	RC	1.34	1.5	0.75	8213
RET-1[a]	3A	RC+CFRP	1.34	1.5	1.5	1044
RET-2[a]	3B	RC+CFRP	1.34	0.92	0.54	5083
UHPFC	D1B	UHPFC	–	0.75	0.5	3433
RUHPFC	D3A	RUHPFC	1.34	1	0.37	20101

[a] CFRP in 2.8 mm strip, one side only.

Table 2
Experimental blast pressure summary [23].

Blast	Charge weight (kg)	Scaled distance to PT1 (m/kg$^{1/3}$)	Peak reflected overpressure (MPa)		Reflected impulse (MPa.ms)	
			PT1	PT2	PT1	PT2
NRC-1	1	3	0.42	0.30	0.186	0.133
NRC-2	8	1.5	2.39	1.0	0.715	0.514
NRC-3	3.4	0.93	6.38	1.49	0.705	0.638
RET-1	1	1.5	2.08	0.89	0.384	0.282

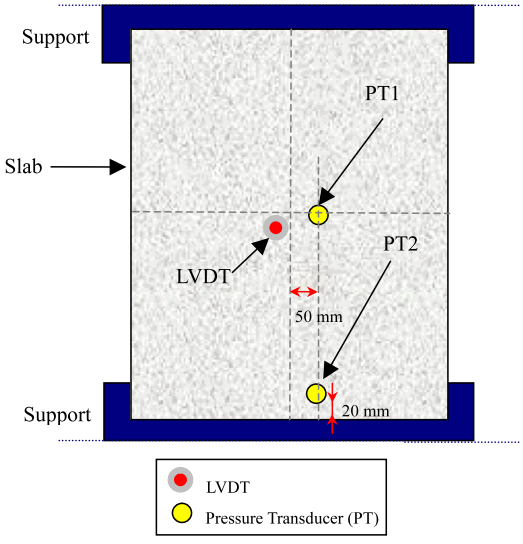

Fig. 6. Slab instrumentation.

2.4. Blast test

Table 1 summarizes the testing program. Test NRC-1 was used to evaluate the instrumentation and was not designed to damage the slab. The standoff distances were measured from the underside of the explosive to the top of the slab.

3. Data recorded from airblasts

3.1. Pressure histories

Airblast pressure histories at the centre and edge of the slabs were recorded to study the pressure distribution on the slabs. Fig. 7 (a) and (b) show the measured pressure histories for NRC-1 and NRC-2 (information on the scaled range is given in the Table 1). As shown, negative pressure was negligible. The overpressure recorded at gauge PT1 was significantly larger than at PT2 in both specimens, indicating that the blast pressure on the slab was not uniform which was an expected result given the small standoff distance. The arrival times of the shock front for PT1 and PT2 also differed considerably for NRC-1 but less so for NRC-2. Two distinct peaks in the pressure history were consistently recorded at pressure gauge PT2, which may be due in part to blast wave reflections off the ground beneath and surrounding the slab. A summary of the blast pressures recorded at PT1 and PT2 and the corresponding impulses are given in Table 2. Since the maximum pressure on the sensors was limited to 6.9 MPa, blast pressure histories for only 4 tests were recorded.

A cylindrically shaped explosive with a diameter to length ratio of 1:1 was used for the experiments; the axis of the cylinder was horizontal as shown in Fig. 8(a). The cylinder of Composition B was detonated with the aid of a booster charge of plastic explosive that was attached to the left end of the cylinder. Based on the damage sustained to the explosive support frame following test RUHPFC, it would appear that the combination of a cylindrically shaped charge and the booster location appeared to focus more energy to the right of the explosive than to the left. Fig. 8(b) is a photograph taken immediately after the detonation for test RET-2. The image shows a jetting effect along the axis of the cylinder.

Only one peak was seen in the PT1 pressure histories as would be expected from a normally reflected shock front. The presence of two peaks in the PT2 pressure histories cannot be explained by an obliquely reflected shock from a free air burst of a spherical charge [24]. Petes and Tempo [25], Ismail and Murray [26], Zimmerman, Nguyen and Hookham [27], and Anderson, Katselis and Caputo [28] reported on the influence of charge shape, cylindrical versus spherical, and on overpressure and impulse. Some of the key findings were:

- Charge orientation can substantially influence peak overpressure and impulse [26].
- For cylindrical charges, peak overpressure and impulse are dependent on the detonation locations. For low ratios of length-to-diameter, more energy is directed in the axial direction and for high length-to-diameter ratios, more energy is directed in the radial direction [27].
- Computational fluid dynamics calculations of blast pressure histories in the near-field do not reproduce experimental data well [28].

Importantly, some of the experimental results presented by Anderson et al. [28] associated with the detonation of cylindrical charges show two peaks in the incident overpressure history which are similar to the reflected pressure histories for gauge PT2 in Fig. 7.

The experimentally recorded reflected overpressures and the reflected impulses computed from the reflected pressure histories were compared with those values predicted using TM5. Results are listed in Table 3. The experimentally measured overpressures were consistently higher than those predicted by TM5 [29], which could

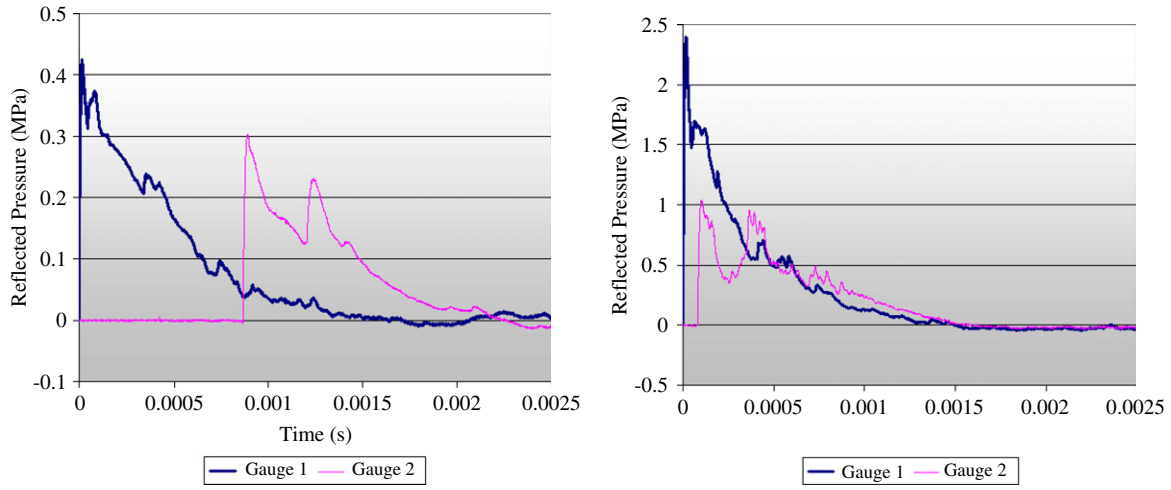

(a) NRC-1. (b) NRC-2.

Fig. 7. Pressure histories on the slabs at PT1 and PT2 [23].

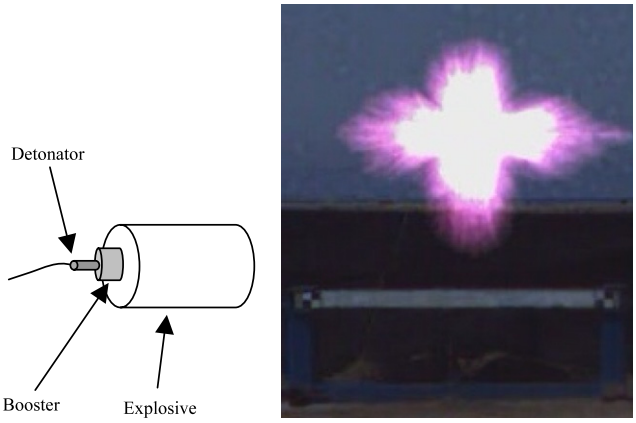

(a) Schematic of cylindrical charge. (b) High speed camera footage of the explosive for test RET-2.

Fig. 8. Influence of charge shape on blast flow field.

Table 3
Experimental and predicted overpressure and impulses for PT1 [23].

Blast	Incident overpressure (MPa)		Reflected overpressure (MPa)		Reflected impulse (MPa.ms)	
	Predicted	Experimental	Predicted	Experimental	Predicted	Experimental
NRC-1	0.07	0.13	0.24	0.42	0.153	0.186
NRC-2	0.45	0.54	1.58	2.39	0.668	0.715
NRC-3	0.34	1.43	6.20	6.38	0.922	0.705
RET-1	0.07	0.12	1.58	2.08	0.334	0.384

be attributed to charge shape as noted previously. The reflected impulses calculated from the experimental data at PT1 were close to the TM5-predicted values.

Using the experimental overpressures reported in Table 2, ratio of the peak overpressures PT1 to PT2 was investigated. The values of the ratio so computed and those calculated using TM5 are presented in Table 4. The differences are substantial and could be attributed to the use of an end-detonated cylindrical charge, small standoff distances and the influence of detonation products.

Using the data from Table 4, it was found that the ratio of the peak pressures was inversely proportional to the scaled distance, as seen in Fig. 9. The following relationship was given by fitting the data.

$$\frac{\mathrm{PT1}}{\mathrm{PT2}} = 3.6Z^{-0.91}. \quad (1)$$

As the relationship is only derived based on data for scaled distances of 1 m/kg$^{1/3}$ and greater, it must be used with caution for scaled distances less than 1.0 and greater than 3.0. The above formula is used to calculate reflected impulses at the PT2 point in Section 5. Importantly, the equation can only be used to compute pressures on the test slabs and is inappropriate for more general use.

3.2. Displacement history

An LVDT was used to record the displacement histories of the slabs. For the first four tests, an adhesive was used to attach the LVDTs to the slab. However, the adhesive connection fared poorly in these tests so that the anchorage was enhanced with concrete anchors for the remaining tests as shown in Fig. 10.

Table 4
Ratios of experimental and predicted overpressures [23].

Blast	Standoff distance to PT1 (m)	Angle of incidence to PT2	Scaled distance to PT1 (m/kg$^{1/3}$)	Measured peak reflected overpressure (MPa)		TM5 peak reflected overpressure (MPa)		PT2 / PT1	
				PT1	PT2	PT1	PT2	Experimental	Predicted
NRC-1	3	16°	3	0.42	0.30	0.33	0.29	0.71	0.88
NRC-2	3	16°	1.5	2.39	1.0	2.52	2.16	0.42	0.86
NRC-3	1.4	32°	0.93	6.38	1.49	9.84	5.32	0.23	0.54
RET-1	1.5	30°	1.5	2.08	0.89	2.53	1.47	0.43	0.58

Table 5
Summary of slab deflections.

Blast	Charge weight (kg)	Standoff distance from PT1 (m)	Scaled distance (m/kg$^{1/3}$)	Max. deflection (mm)	Permanent deflection (mm)
NRC-1	1	3	3	1.5	0
NRC-2	8	3	1.5	10.5	–[a]
NRC-3	3.4	1.4	0.93	13.9	–[a]
NRC-4	8	1.5	0.75	38.9	–[a]
RET-1	1	1.5	1.5	3.3	0
RET-2	5	0.92	0.54	50.6	7.6
UHPFC	3.4	0.75	0.5	13.2	4.1
RUHPFC	20	1	0.37	>100	–[b]

[a] LVDT debonded from the concrete and the permanent deflection was not recorded.
[b] LVDT was destroyed by the test.

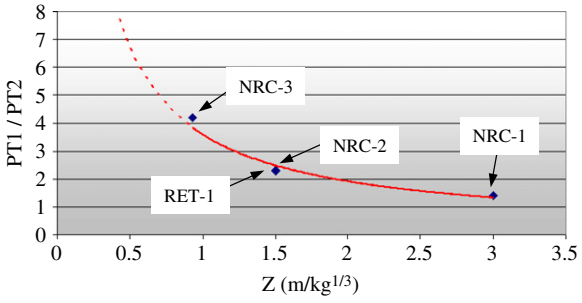

Fig. 9. Relationship between PT1/PT2 and scaled distance [23].

Fig. 10. LVDT connection to the underside of a test specimen.

The LVDT histories were zero-corrected at the start of each test. The deflection histories of NRC-1 and RET-1 in Fig. 11(a) and (b) show permanent deflections of approximately 0.3 mm and 0.5 mm, respectively, that can be attributed to the deformation in the supporting fibre board. This rigid body deflection was removed from the slab displacement history. Residual displacements in the tests that produced no slab damage were removed from the displacement histories. Such displacements were not removed in tests involving slab damage because the contribution due to deformation in the fibre board could not be quantified. A summary of the maximum and residual slab deflections is given in Table 5.

4. Performance of test specimens

4.1. Normal reinforced concrete slabs

A total of four charges with scaled distances ranging from 0.75 m/kg$^{1/3}$ to 3 m/kg$^{1/3}$ as summarized in Table 5 were conducted on two NRC slabs. No cracking was observed in specimens NRC-1 and NRC-2 after testing. Fine cracks of negligible residual width were observed in NRC-3 but it is unlikely that the yield moment in the slab was reached. Fig. 12 shows the cracks marked after the test.

After NRC-4 was subjected to a charge weight of 8 kg at a scaled distance of 0.75 m/kg$^{1/3}$, cracks which were significant in depth and number were developed along the length of the slab. Residual crack widths were measured, indicating a plastic or post-yield response. Fig. 13 shows the crack pattern for NRC-4. As shown, there were no cracks near the supports.

4.2. Retrofitted reinforced concrete slabs

Two NRC slabs retrofitted with two 2.8 mm thick plates of pultruded FRP on the compressive face were exposed to two charges with scaled distances of 1.5 m/kg$^{1/3}$ and 0.54 m/kg$^{1/3}$ as summarized in Table 5. No cracks were observed for RET-1 which was exposed to a charge with a scaled distance of 1.5 m/kg$^{1/3}$ and a charge weight of 1 kg, indicating the slab remained elastic.

Specimen RET-2 was subjected to a 5 kg explosion at a standoff distance of 0.92 m. The resultant damage can be seen in Fig. 14 which includes cracks associated with flexure and shear (highlighted following the test) as well as debonding of the FRP laminates. No concrete crushing was observed.

Fig. 14(a) shows debonding between the top and bottom layers of the CFRP for RET-2. One 100 mm wide plate debonded at the slab centerline and one 40 mm wide plate debonded along the length of the slab (see Fig. 14(a)). Debonding occurred between the CFRP strips and not at the CFRP-concrete interface.

During rapid loading, direct shear cracks can be formed in areas of concentrated loads (reactions) [29]. Such vertical cracks can be seen in Fig. 14(b). Direct shear failures will preclude the development of the flexural strength of a slab and are undesirable, although, probably unavoidable for near-field charges.

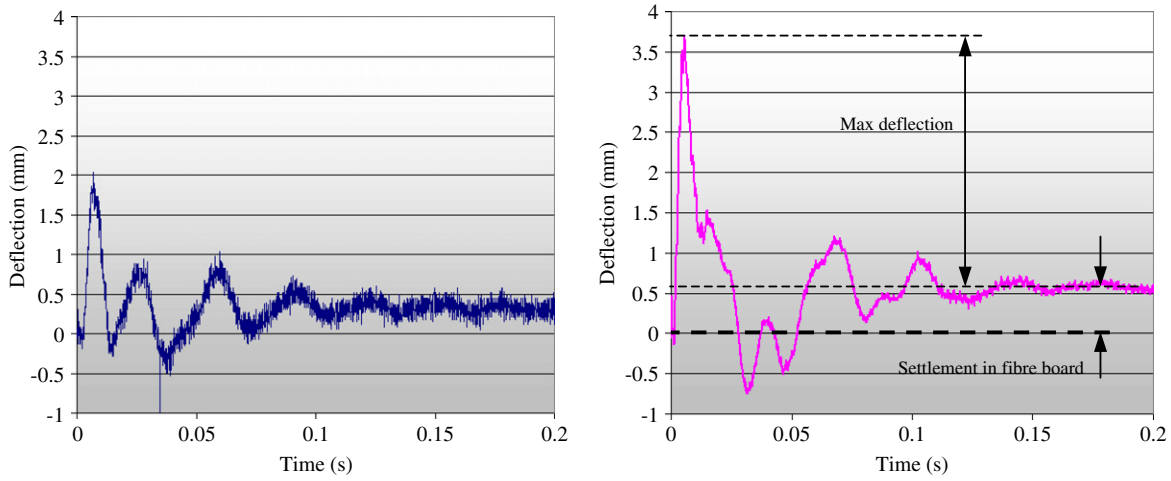

(a) NRC-1. (b) RET-1.

Fig. 11. LVDT displacement histories [23].

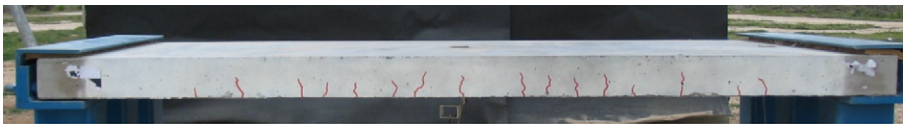

Fig. 12. Cracks in specimen NRC-3.

Fig. 13. Cracks in specimen NRC-4.

4.3. Plain ultra-high performance fibre concrete slab

The plain UHPFC slab survived a charge weight of 3.4 kg and a scaled distance of 1.13 m $kg^{1/3}$ and only flexural cracking was observed in the slab at the mid and quarter points as shown in Fig. 15. The LVDT recorded a permanent deflection of 4.1 mm. This test confirmed the substantial ability of ultra-high performance fibre concrete for resisting blast loads.

4.4. Reinforced ultra-high performance fibre concrete slab

The RUHPFC slab was exposed to a severe blast loading with a charge weight of 20 kg and a scaled distance of 0.37 $mkg^{1/3}$. Concrete crushing was observed in the hinge region at approximately the centre of the span as seen in Fig. 16. The entire deflection history of the blast was not measured completely because the LVDT was destroyed during the test but the maximum recorded deflection exceeded 100 mm. The usefulness of ultra-high performance fibre concrete for blast resistance was further confirmed by this large blast load at a small standoff distance.

5. Energy absorption of specimens

The resistance–deflection relationship of a member is critical for a comparison of blast resistance capacities since the area under the resistance–deflection curve provides a measure of its energy absorption capacity. Assuming that the loading can be considered as an impulse (i.e., $t_d < 0.1T$ where t_d is the fictitious positive phase duration and T is period of the member), the required energy absorption capacity of a member should exceed the imposed demand. The estimated fundamental period of the panels was 29.2 ms specimen. The measured positive phase duration of the loading varied between 0.99 ms (NRC-3) to 1.70 ms (NRC-1), which supported the assumption that the loading was impulsive.

We used SDOF techniques to compute the required energy absorption capacity of the concrete panels and compare energy demand and energy capacity. The equation of motion for the nonlinear SDOF system can be presented in a number of formats, two of which are presented below from [30]:

$$K_m M\ddot{u}(t) + K_L R(t) = K_L P(t) \tag{2}$$

$$K_{LM} M\ddot{u}(t) + R(t) = P(t) \tag{3}$$

where K_M, K_L, and K_{LM} are the mass, load, and load–mass transformation factors, respectively, $u(\ddot{u})$ is the displacement (acceleration) of the single degree of freedom system, M is the total mass of the panel (=440 kg) computed assuming a span of 1800 mm, and R is the resistance of the mass presented in the same units as the load, P. The energy absorption capacity E_n must exceed the applied impulse energy:

$$E_n > \frac{I^2}{2(K_{LM}M)} \tag{4}$$

where I is the total impulse imposed on the panel. The value of K_{LM} for a SDOF system for a simply supported member subjected to a uniformly distributed load and responding far into the inelastic range is 0.72 [30].

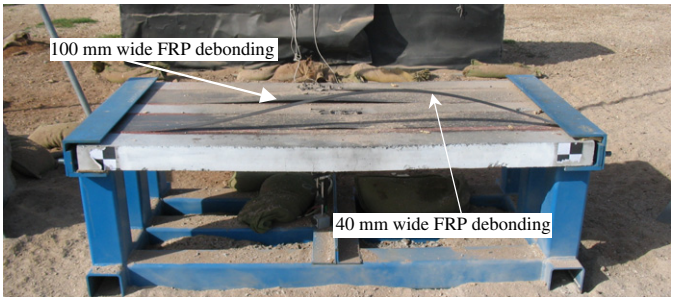

(a) FRP plate debonding.

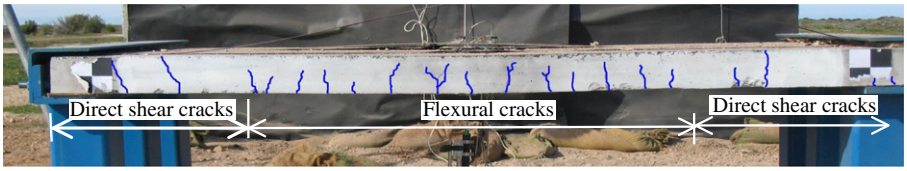

(b) Crack patterns.

Fig. 14. Damage in specimen RET- 2.

Fig. 15. Cracking in the plain UHPFC slab.

Fig. 16. Flexural failure of the RUHPFC specimen.

Based on data from Table 2, the total impulses applied to the NRC-1, NRC-2, NRC-3 and RET-1 specimens were calculated; results are listed in Table 6. For specimens NRC-4, RET-2, UHPFC and RUHPFC, the reflected impulse at PT1 was predicted using TM5. The impulse at PT2 for all specimens was estimated by multiplying the impulse at PT1 by the ratio of PT2/PT1 calculated from Eq. (1). We recognize that this computation is approximate and assumes that the positive phase duration at PT1 and PT2 are identical. The total impulse applied to the panel was computed by multiplying the averaged measured (or computed) specific impulse at PT1 and PT2 by the area of the panel.

The flexural blast resistance of a cross-section of a specimen can be determined using a layered analysis method [22]; this method was used to establish the peak resistance of each panel. In such analyses, the cross-section is divided into a number of layers with the strain, strain rate and stress assumed to be constant within each layer as shown in Fig. 17. This procedure enables the strain rate to be varied over the depth of the cross-section where the strain rate profile that was derived from a previous study [22] was used herein. The flexural resistance of a cross-section is calculated using traditional procedures that first determine the neutral axis depth for a specific curvature. For example for a given specific curvature, the resistance of the ith slice is $F_i = \sigma_i(\varepsilon_i) DIF_i(\dot{\varepsilon}_i) w_b \Delta s$, where $\sigma_i(\varepsilon_i)$ is the stress, $DIF_i(\dot{\varepsilon}_i)$ is the dynamic increase factor that is strain rate dependent, and w_{bi} and Δs_i are the width and thickness of the slice, respectively. The neutral axis depth $k_u d$ is varied until horizontal force equilibrium is achieved and then the moment capacity at that specific curvature can be calculated. The resistance–deflection relationship of the NRC and retrofitted RC specimens was determined per Wu et al. [22] and their energy absorption capacities are shown in Table 6.

As shown in Table 6, although the imposed impulses on NRC-4 and RET-2 were much larger than their maximum energy absorption, both slabs survived the loading. RET-2 was subjected to an impulse of 2445 kN ms; this is 38% greater than the impulse for NRC-4, which indicates that compressive retrofitting greatly increased the blast resistance. The damage to the two slabs was very similar, with large flexural cracks which indicate that both slabs were close to the point of concrete crushing.

Table 6
Resistance, reflected impulses and energy demands and capacities.

Specimen	Charge weight (kg)	Scaled distance (m/kg$^{1/3}$)	Predicted energy absorption capacity (kN mm) E_n	Recorded max. deflection (mm)	Estimated energy absorption (kN mm)	Averaged reflected impulse (kN ms)	Applied impulse energy (kN mm) $\frac{I^2}{2(K_{LM}M)}$
NRC-1	1.0	3.00	3725	1.5	33	287	141
NRC-2	8.0	1.50	3725	10.5	1630	1106	2124
NRC-3	3.4	0.93	3725	13.9	2572	1209	2536
RET-1	1.0	1.50	6730	3.3	192	599	624
NRC-4	8.0	0.75	3725	38.9	$>E_n$	1774	5464
RET-2	5.0	0.54	6730	50.6	$>E_n$	2445	10375
UHPFC	3.4	0.75	2194	13.2	$>E_n$	1335	3089
RUHPFC	20.0	1.00	32339	>100	$>E_n$	7322	93077

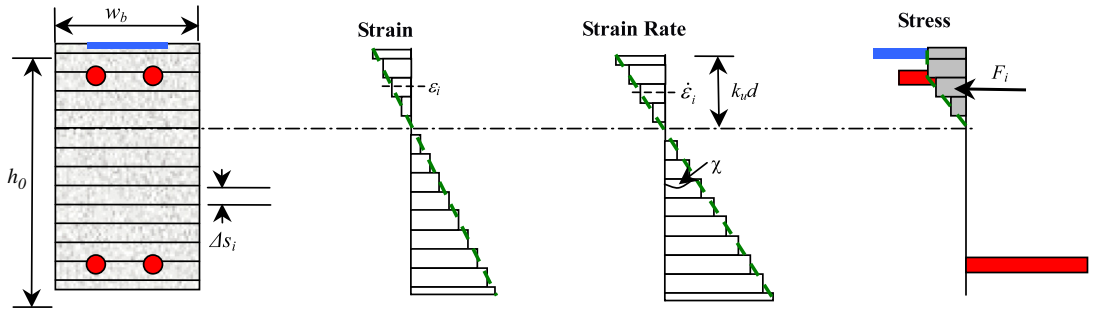

Fig. 17. Layered analysis of a cross-section.

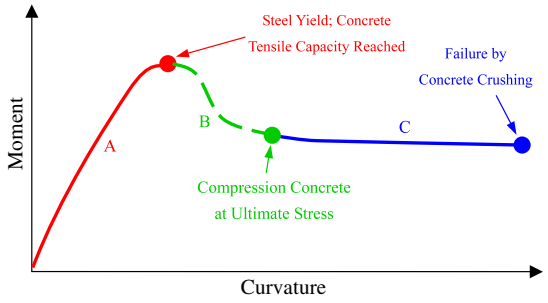

Fig. 18. Moment–curvature relationship for RUHPFC specimen [23].

The use of the stress–strain profile for UHPFC shown in Fig. 1 resulted in a somewhat unusual moment–curvature relationship for the RUHPFC specimen as shown in Fig. 18. For the region A in Fig. 18, the stress distribution of the cross-section in this region is linear elastic as shown in Fig. 19(b). Region B begins after the steel bars in the area of the cross-section in tension reach their yield strain 0.2%. In this region, the neutral axis of the cross-section translates up with increasing curvature, thereby reducing the resisting moment of the cross-section. Region C starts when the compressive stress reaches its maximum value at the extremity, Beyond this point, the cross-section behaves similarly to that of a normal reinforced concrete plastic hinge. With increasing curvature, the concrete compressive stress distribution is close to a rectangular stress block as shown in Fig. 19(d). Eventually, the curvature capacity is exhausted due to crushing of concrete. The moment–curvature relationship of the plain UHPFC specimen was also derived using the stress–strain profiles of the UHPFC shown in Fig. 1.

Table 6 lists the predicted energy absorption based on the recorded maximum deflection, the energy absorption capacity (area under the resistance–displacement relationship) of each panel, and the reflected impulse and associated impulse energy (Eq. (4)). There is a substantial difference between the estimated energy absorption capacity and the corresponding applied blast impulse energy for NRC-1 and RET-1. The estimated energy absorption capacity and the corresponding applied blast impulse energy are similar for NRC-2 and NRC-3. The energy absorption of the specimens was estimated here assuming simple supports, although the end restraint in the field was somewhere between fixed and pinned, where the degree of fixity is likely dependent on the magnitude of the imposed blast load and the damage sustained by the restraints that are shown in Fig. 4(b). Table 6 also shows that the energy absorption capacity of the plain UHPFC specimen is comparable to that of the NRC specimen but that the RUHPFC specimen was superior to both. Figs. 12 and 15 can be used to compare the performance of the NRC slabs with the plain UHPFC slabs. Slab NRC-3 and the plain UHPFC slab were subjected to applied impulse energies of 2,536 kN mm and 3,089 kN mm, respectively. The plain UHPFC specimen suffered less damage than NRC-3 although the demand was larger, which suggests that the plain UHPFC slab was superior to the NRC-3 slab. The RUHPFC specimen was subjected to a much larger blast impulse (approximately 15–20 times greater) than the other slabs which indicates that the ultra-high performance fibre concrete has a very higher energy absorption capacity and is, therefore, a most desirable material for use against blast loads. Importantly, no scabbing nor shear cracking was observed in the RUHPFC slab after testing with a large weapon at close range.

6. Conclusions

A series of blast tests has been carried out to investigate the blast resistance of reinforced concrete slabs constructed with: (a) normal reinforced concrete (NRC); (b) reinforced concrete augmented with FRP plates; (c) ultra-high performance concrete without reinforcement (UHPFC); and (d) ultra-high performance concrete with reinforcement (RUHPFC). Evaluation of pressure histories showed that the use of end-detonated cylindrical charges will produce shock fronts in the near-field that differ substantially from those assumed in TM5 for standard blast design. It is suggested that for testing structural components, centrally detonated spheres of explosives should be used to simplify the flow field calculations as well as the interpretation of test results. Blast

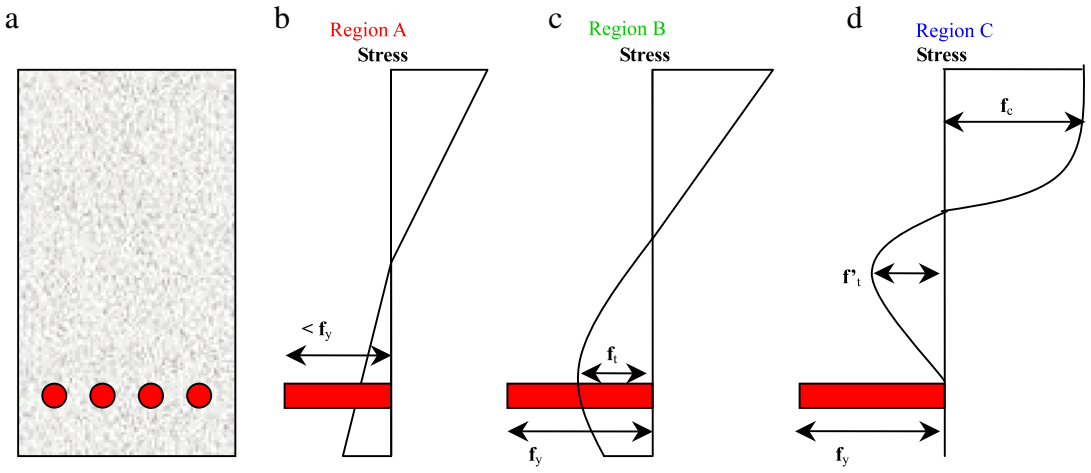

Fig. 19. Stress profiles for different regions of the moment–curvature of Fig. 18 [23].

testing indicated that the plain UHPFC slab suffered less damage than the NRC slabs when subjected to similar blast loads which confirms that UHPFC is a more effective material for blast design. The performance of the RUHPFC slab was superior to all other slab types tested in the program. Adhesive bonding externally bonded FRP material to the compressive face of the NRC slab improved its blast resistance but the percentage improvement could not be quantified because the slabs were not tested to the point of incipient failure.

Acknowledgements

The experimental study was conducted as part of a final year research project by Coppola R, Jones J and Marks S. The technical assistance of staff from the School of Civil, Mining and Environmental Engineering at the University of Adelaide and from the Defence Science and Technology Organisation in Edinburgh, South Australia is gratefully acknowledged as well as VSL Australia Pty Ltd for supplying the UHPFC specimens.

References

[1] Luccioni BM, Ambrosini RD, Danesi RF. Analysis of building collapse under blast loads. Eng Struct 2004;26(1):63–71.
[2] Thompson D, Brown S, Mallonee S, Sunshine D. Fatal and non-fatal injuries among US Air Force personnel resulting from the terrorist bombing of the Khobar Towers. J Trauma-Inj Infect Crit Care; 57(2) 208–15.
[3] Osteraas JD. Murrah building bombing revisited: A qualitative assessment of blast damage and collapse patterns. J Perform Constr Facil; 20(4) 330–5.
[4] Islam AKMA, Yazdani N. Performance of AASHTO girder bridges under blast loading. Eng Struct 2008;30(7):1922–37.
[5] Antoniades KK, Salonikios TN, Kappos AJ, Kappos AJ. Evaluation of hysteretic response and strength of repaired R/C walls strengthened with FRPs. Eng Struct 2007;29(9):2158–71.
[6] Rougier VC, Luccioni BM. Numerical assessment of FRP retrofitting systems for reinforced concrete elements. Eng Struct 2007;29(8):1664–75.
[7] Sheikh SA, Li Y. Design of FRP confinement for square concrete columns. Eng Struct 2007;29(6):1074–83.
[8] Ali MSM, Oehlers DJ, Griffith MC, Seracino R. Interfacial stress transfer of near surface-mounted FRP-to-concrete joints. Eng Struct 2008;30(7):1861–8.
[9] Gee-Joo Ha, Yun-Yong Kim, Chang-Geun Cho. Groove and embedding techniques using CFRP trapezoidal bars for strengthening of concrete structures. Eng Struct 2008;30(4):1067–78.
[10] Parra-Montesinos GJ, Peterfreund SW, Chao SH. Highly damage-tolerant beam–column joints through use of high-performance fiber-reinforced cement composites. ACI Struct J 2005;102(3):487–95.
[11] Magnussen J, Hallgren M. Reinforced high strength concrete beams subjected to air blast loading. In: Structures and materials, v 15, structures under shock and impact VIII. 2004. p. 53–62.
[12] Luo X, Sun W, Chan SYN. Impact resistance of high-strength fibre-reinforced concrete. Mag Concr Res 2007;59(3):199–210.
[13] Rebentrost M, Wight G. Experience with UHPC in Asia. In: 2nd International conference on ultra-high performance concrete. 2008.
[14] Rebentrost M, Cavill B. Reactive powder concrete bridges. In: 6th AustRoads bridge conference. 2006.
[15] Ngo T, Mendis P, Krauthammer T. Behavior of ultrahigh-strength subjected to prestressed concrete panels blast loading. J Struct Eng Amer Soc Civil Eng 2007; 133(11):1582–90.
[16] Ross CA, Purcell MR, Jerome EL. Blast response of concrete beams and slabs externally reinforced with fibre reinforced plastics (FRP). In: Proceedings of the XV structures congress. 1997. p. 673-7.
[17] Muzsynski L, Purcell M. Composite reinforcement to strengthen existing structures against airblast. J Comp Constr 2003;7:93–7.
[18] Lu B, Silva P, Nanni A, Baird J. Retrofit for blast-resistant RC Slabs with composite materials. Missouri: University of Missouri-Rolla; 2006.
[19] Wu C, Oehlers DJ, Wachl J, Glynn C, Spencer A, Matthew M, Day I. Blast testing of RC slabs retrofitted with NSM CFRP plates. Adv Struct Eng 2007;10(4): 397–414.
[20] Cramsey N, Naito C. Analytical assessment of blast resistance of precast prestressed concrete components. PCI J 2007;67–79.
[21] Hyde DW. User's guide for microcomputer program CONWEP. Application of TM5-855-1. Fundamental of protective design for conventional weapons, Instruction report SL-88-1. Vicksburg (MI): Structures Laboratory, US Army Waterways Experiment Station; 1992.
[22] Wu C, Oehlers DJ, Day I. Layered blast capacity analysis of FRP retrofitted RC members. Adv Struct Eng [in press].
[23] Coppola R, Jones J, Marks S. Resistance against Explosive Loading of Ultra High strength and Externally Bonded FRP Retrofitted RC Structural Members. Final year research project report. Adelaide (Australia): School of Civil and Environmental Engineering, The University of Adelaide; 2007.
[24] Baker WE. Explosions in air. Austin: University of Texas Press; 1973.
[25] Petes J, Tempo K. Handbook of HE explosion effects. DNA Report DASIAC-TN-86-15. Washington (DC): Defense Nuclear Agency; 1986.
[26] Ismail MM, Murray SG. Study of the blast waves from the explosion of nonspherical warheads, propellants, explosives. Pyrotechnics 1993;18: 132–138.
[27] Zimmerman HD, Nguyen CT, Hookham PA. Investigation of spherical vs cylindrical shape effects on peak free-air overpressure and impulse. In: Proceedings, 9th international symposium on interaction of the effects of munitions with structures; 1999.
[28] Anderson JG, Katselis G, Caputo C. Analysis of a generic warhead part I: Experimental and computational assessment of free field overpressure. DSTO Technical report 1313. Edinburgh (South Australia): Defence Science and Technology Organisation, Australian Department of Defence; 2002.
[29] Department of Defence (DoD). Structures to resist the effect of accidental explosions. Navy and Air Force technical manual, TM5-1300, Washington (DC): US Department of the Army; 1990.
[30] Biggs J. Introduction to structural dynamics. McGraw-Hill; 1964.
[31] Tolba AFF. Response of FRP-retrofitted reinforced concrete panels to blast loading. http://www.civeng.carleton.ca/Students/Alumni/Show.php3?student=605, available from 31 May 2005.